Supplementary Information (SI)

Flash pulse heating synthesis of gel-derived $CoNiO_x$ nanoclusters for efficient H_2O_2 electrosynthesis in neutral media

Siyi Lin[1], Xiaotong Liu[1], Yuanting Liu[1], Zhaoyu Jin[2], Panpan Li[1*]

[1] College of Materials Science and Engineering, Sichuan University, Chengdu 610065, P. R. China;
[2] Institute of Fundamental and Frontier Sciences, University of Electronic Science and Technology of China, Chengdu 611731, P. R. China;
*E-mail: panpanli@scu.edu.cn

Experimental Section

Chemicals and materials

Nickel(II) chloride hexahydrate ($NiCl_2 \cdot 6H_2O$), potassium hexacyanocobaltate(III) ($K_3[Co(CN)_6]$), pyrrole (C_4H_5N), cobalt(II) chloride hexahydrate ($CoCl_2 \cdot 6H_2O$), potassium tetracyanonickelate(II) ($K_2[Ni(CN)_4]$), ammonium persulfate ($(NH_4)_2S_2O_8$), sodium sulfate (Na_2SO_4), isopropanol (C_3H_8O), hydrochloric acid (HCl), and absolute ethanol (C_2H_6O) were purchased from Chengdu Kelong Chemical Co., Ltd. (Chengdu, China). Nafion solution (5 wt%) was purchased from Shanghai Hesen Electric Co., Ltd. (Shanghai, China).

Catalyst preparation

1. Synthesis of hydrogel precursors.

Pyrrole monomer (0.3 M) and nickel(II) chloride hexahydrate ($NiCl_2 \cdot 6H_2O$) were dissolved in deionized water under ultrasonication to obtain Solution A (15 mL). Potassium hexacyanocobaltate(III) ($K_3[Co(CN)_6]$) and ammonium persulfate ($(NH_4)_2S_2O_8$, 0.3 M) were dissolved in deionized water under ultrasonication to obtain Solution B (15 mL). Solution A was rapidly poured into Solution B, and the resulting mixture was kept overnight to ensure complete polymerization. To evaluate the effect of the Ni/Co ratio, a series of catalysts with Ni/Co molar ratios of 1:2, 1:1, 2:1, 4:1, 6:1, and 8:1 were prepared by varying the molar ratio of $NiCl_2 \cdot 6H_2O$ to $K_3[Co(CN)_6]$, while keeping the total metal precursor concentration constant at 0.2 M. The resulting samples were denoted as $CoNiO_x$ (1:2), $CoNiO_x$ (1:1), $CoNiO_x$ (2:1), $CoNiO_x$ (4:1), $CoNiO_x$ (6:1), and $CoNiO_x$ (8:1). For comparison, NiO_x and CoO_x were synthesized using the same procedure, except that the bimetallic precursors were replaced with the corresponding monometallic precursor alone (i.e., $NiCl_2 \cdot 6H_2O$ and $K_2[Ni(CN)_4]$ for NiO_x or $CoCl_2 \cdot 6H_2O$ and $K_3[Co(CN)_6]$ for CoO_x). A metal-free PPy hydrogel was also synthesized by omitting $NiCl_2 \cdot 6H_2O$ and $K_3[Co(CN)_6]$ from the precursor solutions.

2. Synthesis of $CoNiO_x$, NiO_x and CoO_x nanoclusters.

The precursors were freeze-dried, and the resulting aerogels were ground into the powders. The powders were calcined in an ultrafast high-temperature furnace (Ultrafast High Temperature Furnace 2022A-8, Particle Precision Instruments Co. Ltd., Jilin Province) under a flowing Ar atmosphere. The calcination involved two stages: in the first stage, the sample (15 mg) was heated to 500 °C and held for 300 s. In the second stage, it was set to 10 pulses (0.1 s on / 1 s off, 10 pulses), reaching a stable pulse temperature of 2100 °C (The temperature was monitored by using an infrared probe integrated and heating rate is approximately 45,000 °C s^{-1}). Then, the final metal oxide catalysts were obtained after this process.

Material characterization

Field-emission scanning electron microscopy (FESEM) images were acquired using a Helios G4 UC microscope. High-angle annular dark-field scanning transmission electron microscopy (HAADF-STEM) images were obtained using a probe-corrected JEOL NEOARM microscope. X-ray diffraction (XRD) patterns were recorded on a Rigaku Ultima IV diffractometer (40 kV, 40 mA) over the 2θ range of 10-80° at a scan rate of 10° min^{-1}. X-ray photoelectron spectroscopy (XPS) measurements were carried out on a Thermo Scientific K-Alpha spectrometer. X-ray absorption near-edge structure (XANES) and extended X-ray absorption fine structure (EXAFS) spectra were collected using a RapidXAFS 1M Plus spectrometer (Anhui Absorption Spectroscopy, China).

Electrochemical measurements

Electrochemical tests were performed on an Autolab PGSTAT M204 workstation using a three-electrode configuration. A rotating ring-disk electrode (RRDE) (IPS-RRDE, Aipusi, Germany) served as the working electrode, a saturated calomel electrode (SCE, 1 M KCl) was used as the reference electrode, and a Pt plate was used as the counter electrode. Before RRDE measurements, the electrode was polished with 0.05 μm α-Al_2O_3 powder to remove surface contaminants. Prior to measurements, O_2 was bubbled through 0.1 M Na_2SO_4 for 30 min to saturate the electrolyte. Unless otherwise noted, the rotation rate was set to 1600 rpm, the ring potential was held at 1.5 V vs. RHE, and linear sweep voltammetry (LSV) was recorded from +0.9 to -0.3 V vs. RHE with the scan rate of 10 mV s^{-1}.

Catalyst ink was prepared by dispersing 4 mg catalyst in a mixture of 40 μL Nafion solution (5 wt%), 720 μL deionized water and 260 μL isopropanol, followed by ultrasonication for 30 min. Then, 8 μL of the ink was drop-cast onto the glassy carbon disk and dried at room temperature. The diameter of disk electrode was 5 mm.

RRDE performance

The RRDE collection efficiency (N) was determined to be 0.32 using a redox probe solution containing 2 mM potassium ferricyanide. The H_2O_2 selectivity and electron transfer number (n) were calculated from the disk current (I_d) and ring current (I_r) as follows:

$$H_2O_2 \text{ selectivity } (\%) = 200 \times I_r / (N \times I_d + I_r) \tag{1-1}$$

$$n = 4 \times I_d / (I_d + I_r / N) \tag{1-2}$$

The kinetic current density (j_k) was calculated using the Koutecky–Levich relationship:

$$1 / j = 1 / j_k + 1 / j_L \tag{1-3}$$

$$j_L = 0.2nFD_0^{2/3}\nu^{-1/6}C_0\omega^{1/2}=B\omega^{1/2} \tag{1-4}$$

, where j is the measured current density on the disk, j_L is the diffusion-limited current density, ω is the rotation rate, n is the electron transfer number, and F is the Faraday constant. D_0 is the diffusion coefficient of O_2 in the electrolyte (1.9×10^{-5} cm^2 s^{-1}), ν is the kinematic viscosity (0.89×10^{-2} cm^2 s^{-1}), C_0 is the bulk concentration of dissolved O_2 (1.2×10^{-3} mol L^{-1}), and B equals to $0.2nFD_0^{2/3}\nu^{-1/6}C_0\omega^{1/2}$. The partial kinetic current for H_2O_2 production at 0.3 V vs. RHE was obtained as follows:

$$j_k(H_2O_2) = j_k \times H_2O_2 \text{ selectivity } (\%) / 100 \quad (1\text{-}5)$$

H_2O_2 production measurement

A flow-cell setup was employed for H_2O_2 electrosynthesis on an Autolab PGSTAT M204 workstation. A three-electrode configuration was used with an SCE (1 M KCl) reference electrode and a Pt plate counter electrode. Catalyst-coated carbon paper (HCP121, 1 cm^2) served as the working electrode. The catalyst dispersion was prepared by dispersing 10 mg of catalyst into a mixture containing 750 μL of water, 200 μL of isopropanol and 50 μL of Nafion solution (5 wt%), followed by the ultrasonication for 2 h. The final mass loading of catalysts was 1 mg cm^{-2}. Unlike the RRDE measurements performed in 0.1 M Na_2SO_4, the flow-cell tests were conducted in 1 M Na_2SO_4 to provide higher ionic conductivity and reduce ohmic losses under high-current operation. O_2 was supplied at a flow rate of 40 mL min^{-1}, and the electrolyte was saturated with O_2 for 30 min prior to all measurements. Galvanostatic electrolysis (I-t) was carried out for 30 min. Potentials were converted to the RHE as follows:

$$E(RHE) = E(SCE) + 0.059 \times pH + 0.240 \text{ V} \quad (1\text{-}6)$$

H_2O_2 quantification by Ce^{4+} redox titration (UV-Vis). Standard Ce^{4+} solutions (0.01, 0.05, 0.1, 0.2 and 0.5 mM) were prepared and characterized by UV-Vis spectroscopy to construct a concentration-absorbance calibration curve. An aliquot of the electrolyte was mixed with a 0.5 mM Ce^{4+} solution at a volume ratio of 1:100, and the mixture was kept for 2 h to ensure complete reaction before UV-Vis measurement. A blank control was prepared under identical conditions using fresh electrolyte without electrolysis. The H_2O_2 concentration was calculated based on the change in Ce^{4+} concentration as follows:

$$2Ce^{4+} + H_2O_2 \rightarrow 2Ce^{3+} + 2H^+ + O_2 \quad (1\text{-}7)$$

$$C(H_2O_2) = ((C_0 - C_x) / 2) \times (V_1 / V_2) \quad (1\text{-}8)$$

where V_1 (L) is the total volume of the mixed solution containing the catholyte aliquot and the Ce^{4+} solution, C_0 and C_x (mol L^{-1}) are the Ce^{4+} concentrations before and after reaction, respectively, and V_2 (L) is the volume of the catholyte aliquot added to the Ce^{4+} solution.

DFT Calculation

All DFT calculations were carried out using the $DMol^3$ package, employing spin-polarized generalized gradient approximation (GGA) with the Perdew-Burke-Ernzerhof (PBE) functional.[1,2] In addition, the empirical DFT-D method was adopted for dispersion correction.[3,4] To model the $CoNiO_x$ catalyst, a Ni-doped cobalt oxide supercell was employed. Before the energy calculation, each atom was geometrically optimized to reduce its energy and force to 1×10^{-6} eV and 0.01 eV $Å^{-1}$, respectively. For all calculations, a real-space global orbital cutoff radius of 4.7 Å and a 3×3×2 k-point grid was used. The solvation effects were considered using the conductor-like screening model (COSMO).[5,6] Based on the standard hydrogen electrode (SHE) model, the free energy (ΔG) was calculated using the following equation:

$$\Delta G = \Delta E + \Delta E_{ZPE} - T\Delta S - neU$$

ΔE represents the reaction energy, ΔEZPE is zero-point energy, $T\Delta S$ is the entropic contribution at the temperature T (298.15 K), U refers to the applied bias and n is the electron transfer number involved in the reaction.

The elementary steps of the ORR on $CoNiO_x$ catalyst were simulated via the following pathways:
Four-electron ($4e^-$) pathway:

$O_2 + * + H^+ + e^- \rightarrow *OOH$

$*OOH + H^+ + e^- \rightarrow *O + H_2O$

$*O + H^+ + e^- \rightarrow *OH$

$*OH + H^+ + e^- \rightarrow H_2O + *$

Two-electron ($2e^-$) pathway:

$O_2 + * + H^+ + e^- \rightarrow *OOH$

$*OOH + H^+ + e^- \rightarrow H_2O_2 + *$

where * represents the active adsorption site on $CoNiO_x$.

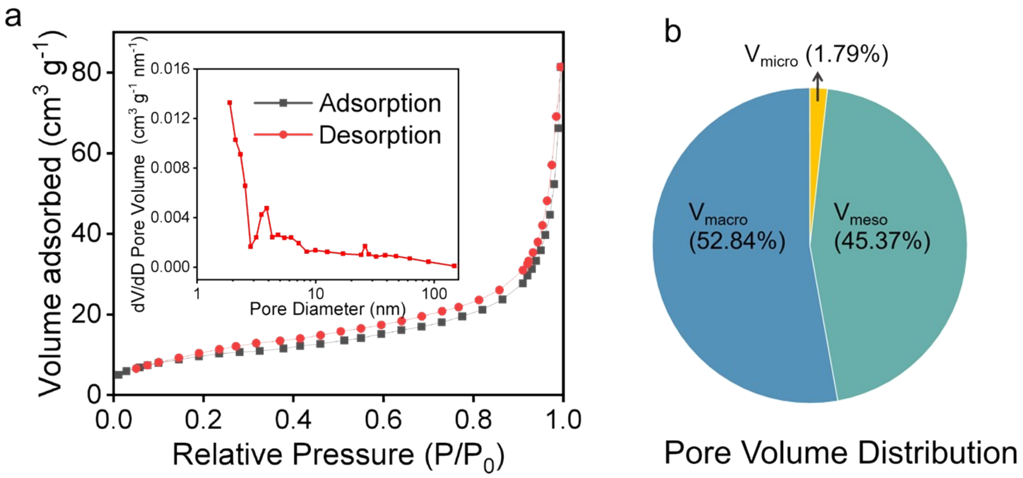

Figure S1. (a) N_2 adsorption-desorption isotherms of $CoNiO_x$ (4:1) (inset: pore-volume distribution). (b) Corresponding pore-size distribution.

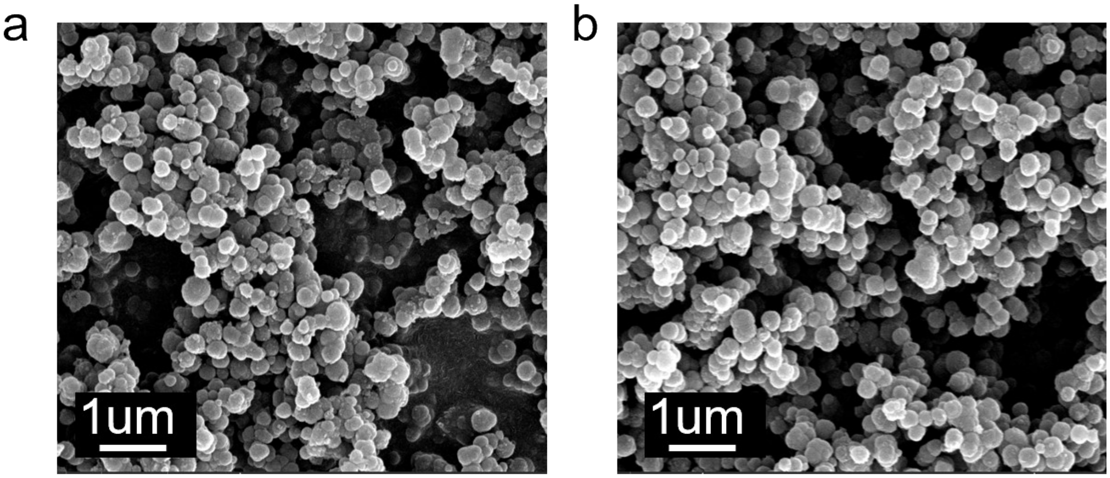

Figure S2. SEM images of (a) NiO_x (b) CoO_x.

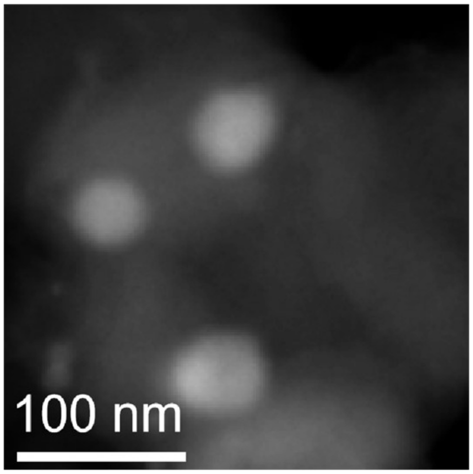

Figure S3. HAADF-STEM image of $CoNiO_x$ (4:1).

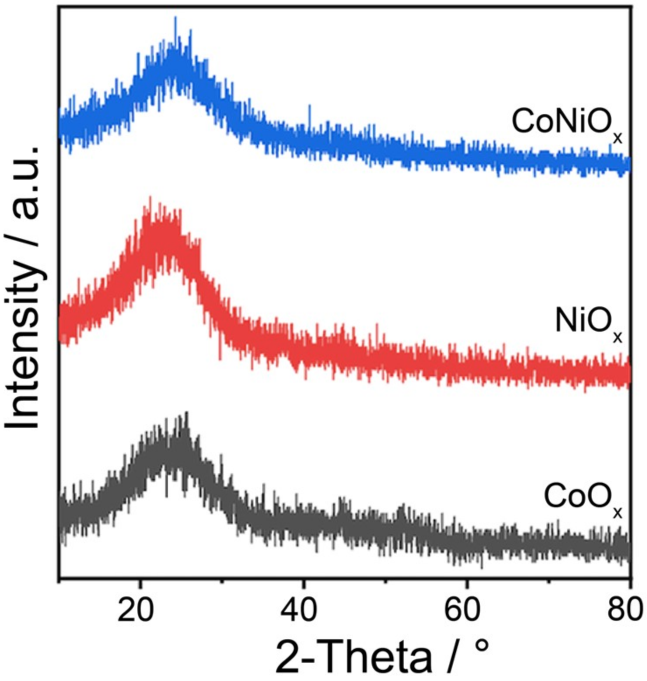

Figure S4. XRD patterns of CoNiO$_x$, NiO$_x$ and CoO$_x$.

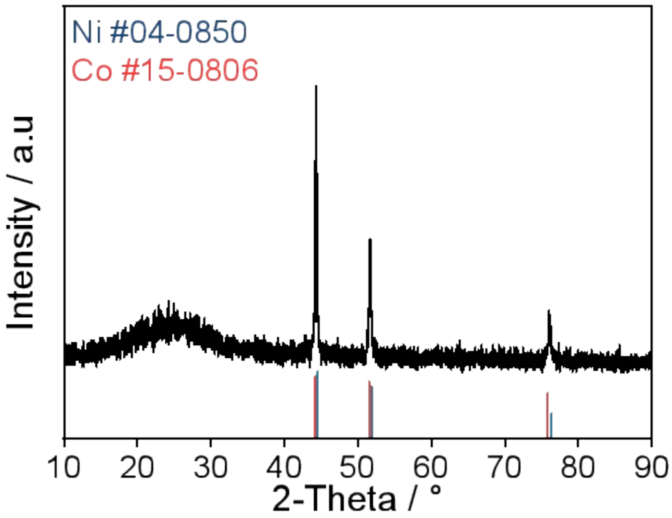

Figure S5. XRD pattern of $CoNiO_x$ catalysts (Control samples were prepared by conventional furnace heating (tube furnace, 800 °C for 2 h)).

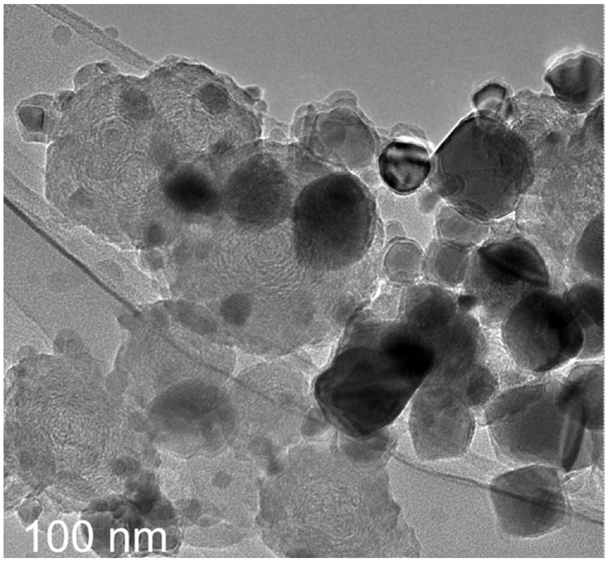

Figure S6. TEM image of $CoNiO_x$ after conventional heat treatment (800 °C, 2 h).

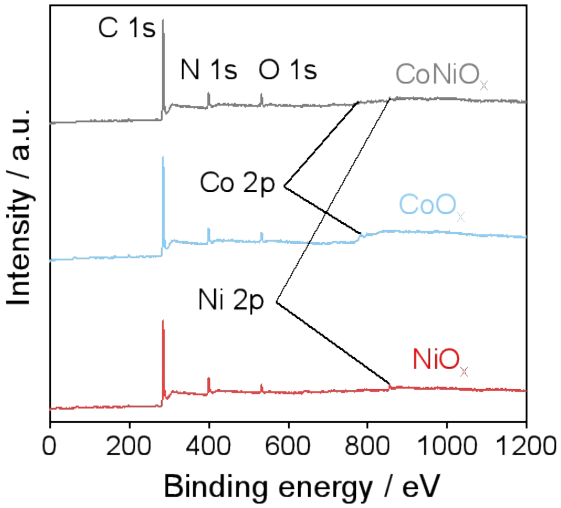

Figure S7. XPS survey spectra of CoNiO$_x$, NiO$_x$ and CoO$_x$.

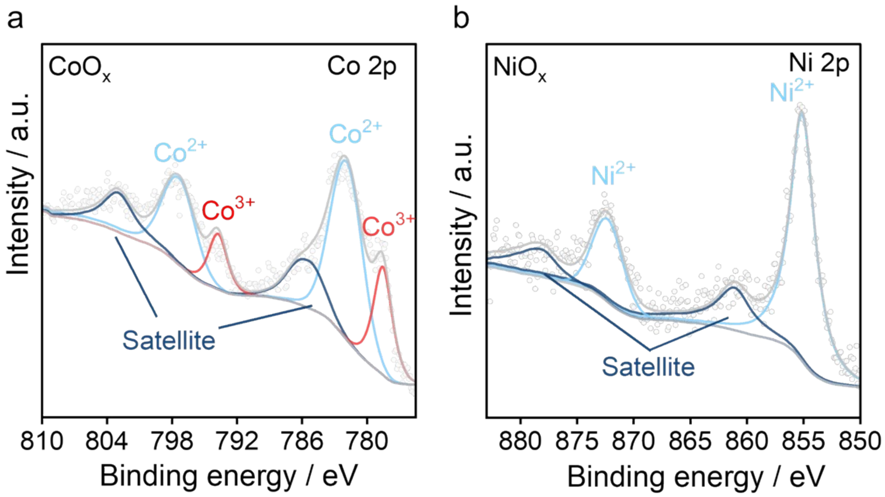

Figure S8. The Co 2p XPS spectra of (a) CoO$_x$ and Ni 2p XPS spectra of (b) NiO$_x$.

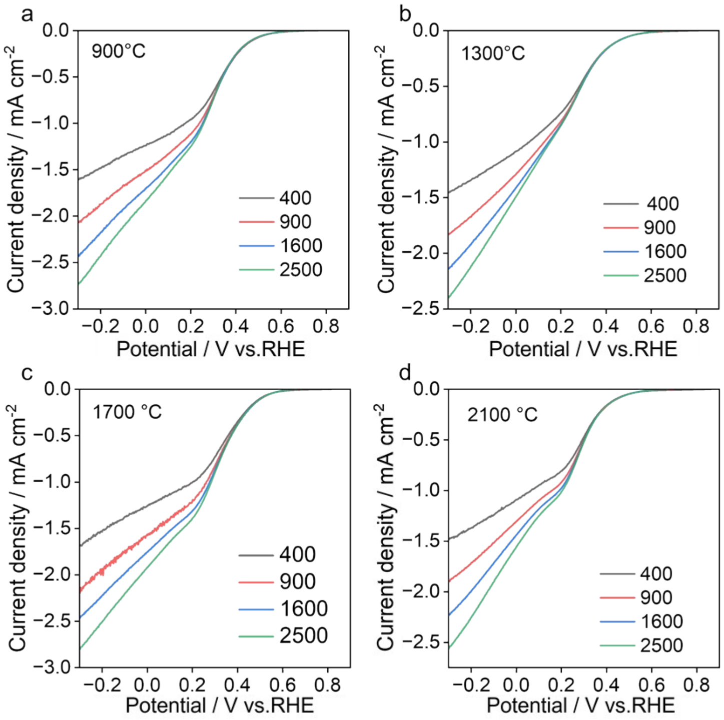

Figure S9. LSV curves of CoNiO$_x$ catalysts calcined at different temperatures (a) 900 °C, (b) 1300 °C, (c) 1700 °C and (d) 2100 °C for electrochemical ORR testing at various rotation speeds.

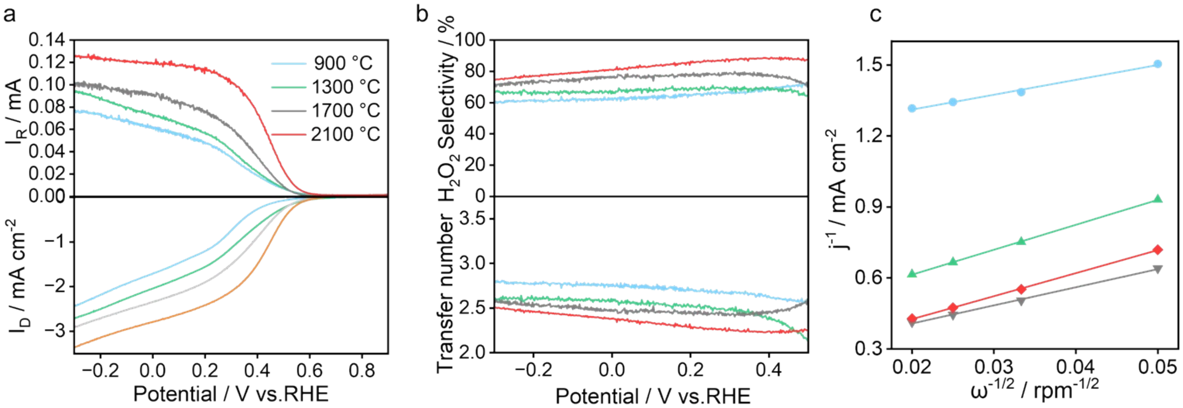

Figure S10. Corresponding (a) ORR polarization curves, (b) H_2O_2 selectivity and electron number and (c) Koutecky-Levich plots at 0.3 V vs. RHE of $CoNiO_x$ at different temperatures (900 °C, 1300 °C，1700 °C，2100 °C).

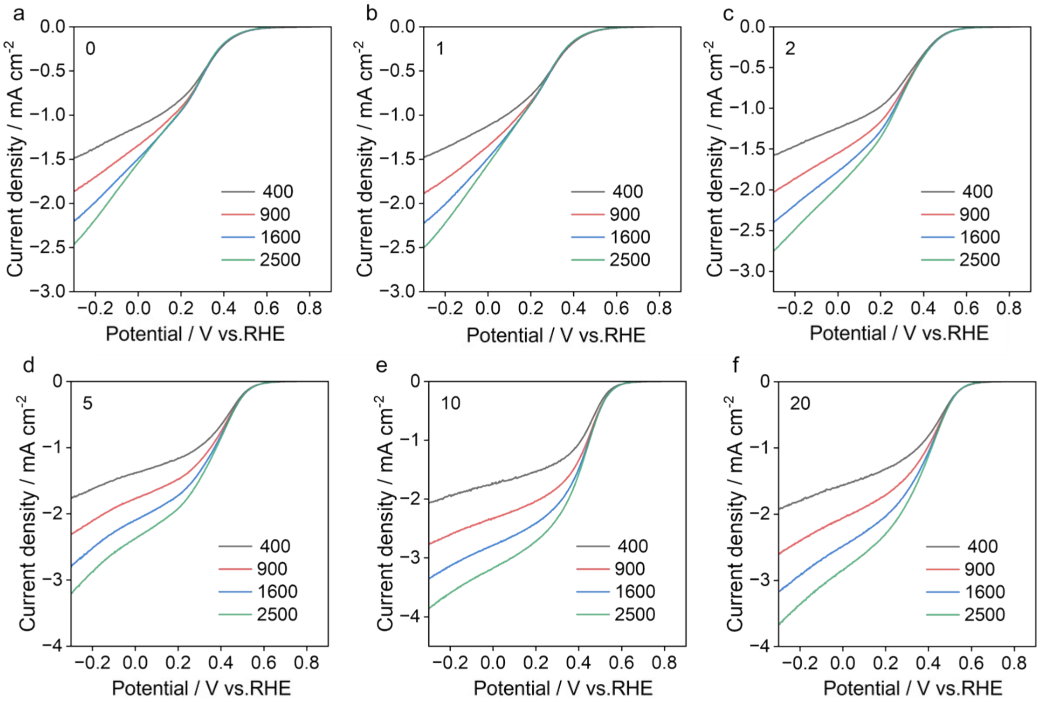

Figure S11. LSV curves of $CoNiO_x$ catalysts synthesis at different pulse times (a) 0 pulse, (b) 1 pulse, (c) 2 pulses, (d) 5 pulses, (e) 10 pulses and (f) 20 pulses for electrochemical ORR testing at various rotation speeds.

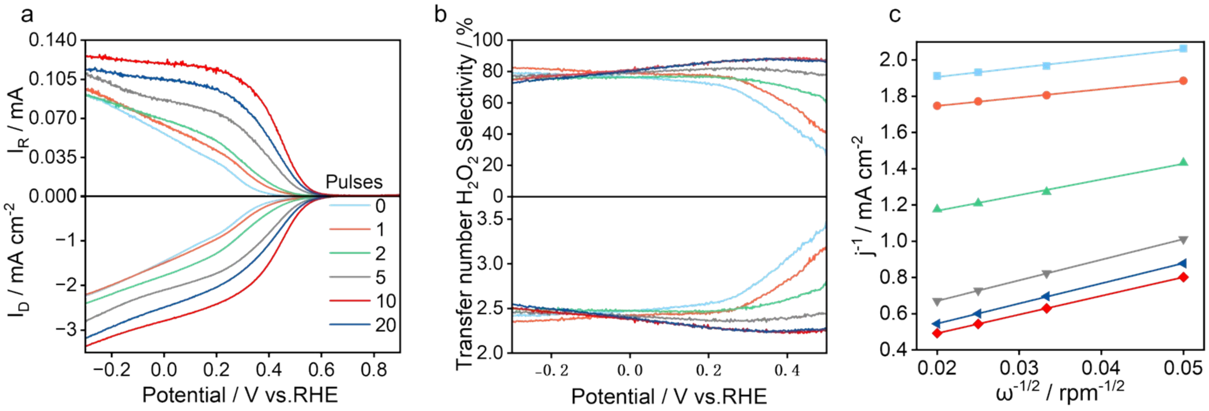

Figure S12. Corresponding (a) ORR polarization curves, (b) H_2O_2 selectivity and electron number and (c) Koutecky-Levich plots at 0.3 V vs. RHE of $CoNiO_x$ at different pulse times (0, 1, 2, 5, 10, 20).

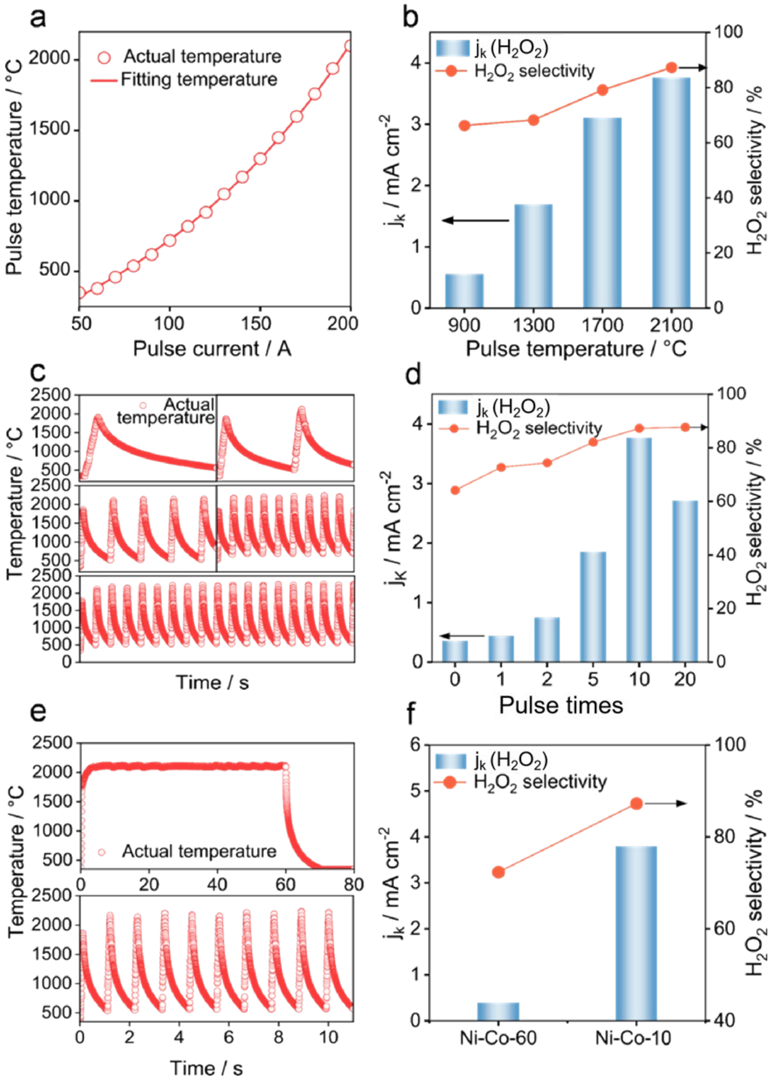

Figure S13. (a) Relationship between pulse current and pulse peak temperature. (b) Corresponding H_2O_2 selectivity and j_k (H_2O_2) at 0.3 V vs. RHE for $CoNiO_x$. (c) Pulse-temperature profiles obtained with different pulse durations at the same peak temperature (0.1 s per pulse). (d) Corresponding H_2O_2 selectivity and j_k (H_2O_2) at 0.3 V vs. RHE for $CoNiO_x$. (e) Comparison of the temperature profiles for long-duration heating and pulsed heating (10 pulses, 0.1 s per pulse). (f) Corresponding H_2O_2 selectivity and j_k (H_2O_2) at 0.3 V vs. RHE for $CoNiO_x$.

A millisecond-resolved flash pulse heating synthesis strategy is employed to construct $CoNiO_x$ active architectures for efficient electrochemical H_2O_2 production in 0.1M Na_2SO_4. The influence of pulse peak temperature on catalytic performance was evaluated using $CoNiO_x$ (4:1) as a model catalyst. With the single-pulse duration (0.1 s) and pulse number fixed, the peak temperature was set to 900, 1300, 1700, and 2100 °C. RRDE measurements show that both disk and ring currents increase monotonically with increasing peak temperature, accompanied by enhanced H_2O_2 selectivity and an electron-transfer number (n) that approaches 2.0. At 0.30 V vs. RHE, the sample treated at 2100 °C exhibits the highest H_2O_2 selectivity and kinetic current density $j_k(H_2O_2)$ (Figure S9, S10, S13a, and S13b). The enhancement in $2e^-$-ORR activity and selectivity is strongly correlated with the peak temperature. In view of the characteristics of high temperature shock, higher peak temperatures are inferred to facilitate transient migration and rearrangement of metal species, while rapid quenching suppresses long-range diffusion and coarsening, thereby enriching $CoNiO_x$ motifs associated with the $2e^-$ ORR pathway.

When the peak temperature and single-pulse duration are fixed, the pulse number reflects the repetition of the high-temperature-activation / rapid-quenching cycle, the cumulative thermal-shock intensity. During each on state, transient activation energy is supplied for metal-species migration and structural reorganization, whereas the subsequent off state rapidly decreases the temperature and reduces the probability of long-range diffusion and coarsening under continuous high-temperature exposure. At a fixed peak temperature of 2100 °C and a pulse duration of 0.1 s, a series of catalysts subjected to different pulse times (0, corresponding to 500 °C pre-annealing only, and 1, 2, 5, 10, and 20 pulses) was prepared. With increasing pulse time, the ORR onset potential shifts positively and the disk/ring currents increase concomitantly, reaching a maximum at 10 pulses (Figure S11-S12). At 0.30 V vs. RHE, $CoNiO_x$ (10 pulse times) delivers an H_2O_2 selectivity of 88.9% and the highest j_k (H_2O_2) in this series (3.80 mA cm^{-2}) (Figures S13c and S13d). In contrast, $CoNiO_x$ subjected only to pre-annealing displays markedly lower current density and selectivity, indicating that, in the absence of ultrahigh-temperature transient activation and intermittent quenching, metal species cannot be sufficiently re-dispersed and structurally optimized, which is unfavorable for generating highly dispersed, high-density $CoNiO_x$ domains. A comparison between millisecond-resolved flash pulse heating synthesis and conventional thermal treatment further shows that samples obtained by conventional heating exhibit significantly lower disk/ring currents over the entire potential window, a more negative ORR onset potential, and an almost one-order-of-magnitude decrease in j_k (H_2O_2) at 0.30 V vs. RHE (Figures S13e and S13f). Prolonged continuous ultrahigh-temperature treatment is more prone to induce structural coarsening of metal clusters, thereby deteriorating the activity and selectivity of the $2e^-$ ORR.

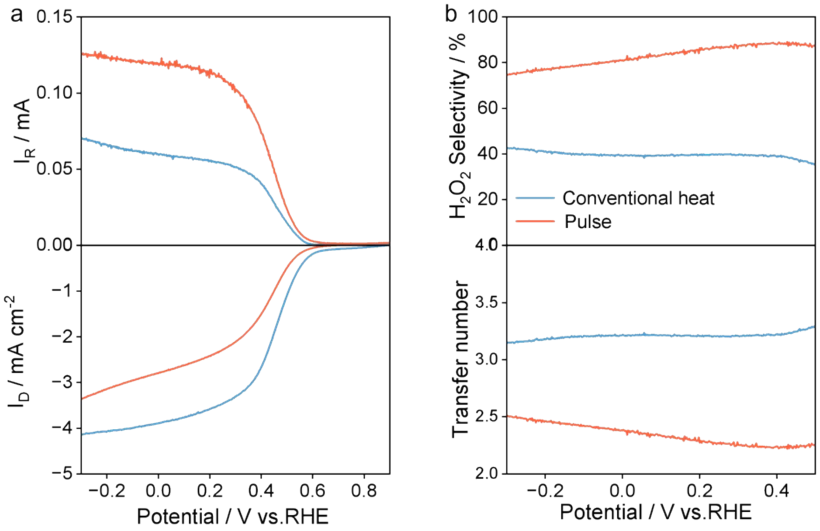

Figure S14. (a) Disk and ring currents of $CoNiO_x$ measured by RRDE. (b) H_2O_2 selectivity and electron-transfer number of $CoNiO_x$. (Control samples were prepared by conventional furnace heating (tube furnace, 800 °C for 2 h).

The conventional heat treatment sample exhibits a higher disk current density, whereas the pulse-synthesized catalyst shows a markedly higher ring current density. These results indicate that the pulse-heated sample favors H_2O_2 production. Accordingly, the pulse-heated sample achieves a maximum H_2O_2 selectivity of 88.90%, significantly higher than that of the conventional heat treatment sample (45%) (Figure S14).

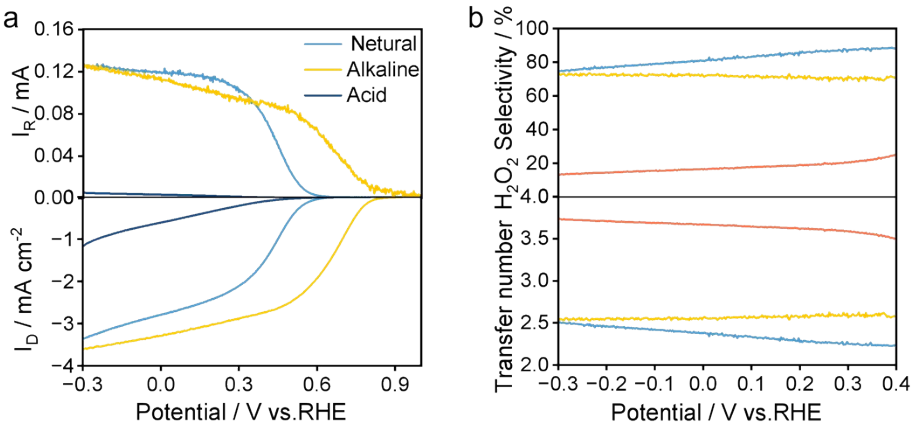

Figure S15. Corresponding (a) ORR polarization curves, (b) H_2O_2 selectivity and electron number of $CoNiO_x$ (4:1) catalysts.

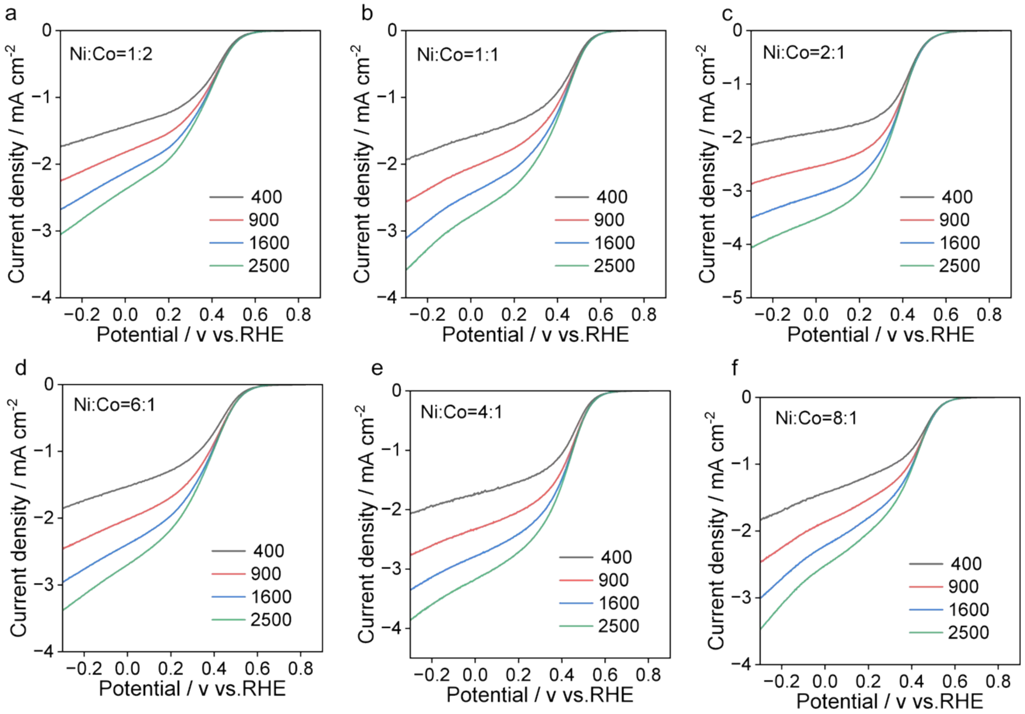

Figure S16. LSV curves of CoNiO$_x$ catalysts with different Ni/Co ratios (a) CoNiO$_x$ (1:2), (b) CoNiO$_x$ (1:1), (c) CoNiO$_x$ (2:1), (d) CoNiO$_x$ (4:1), (e) CoNiO$_x$ (6:1) and (f) CoNiO$_x$ (8:1) for electrochemical ORR testing at various rotation speeds.

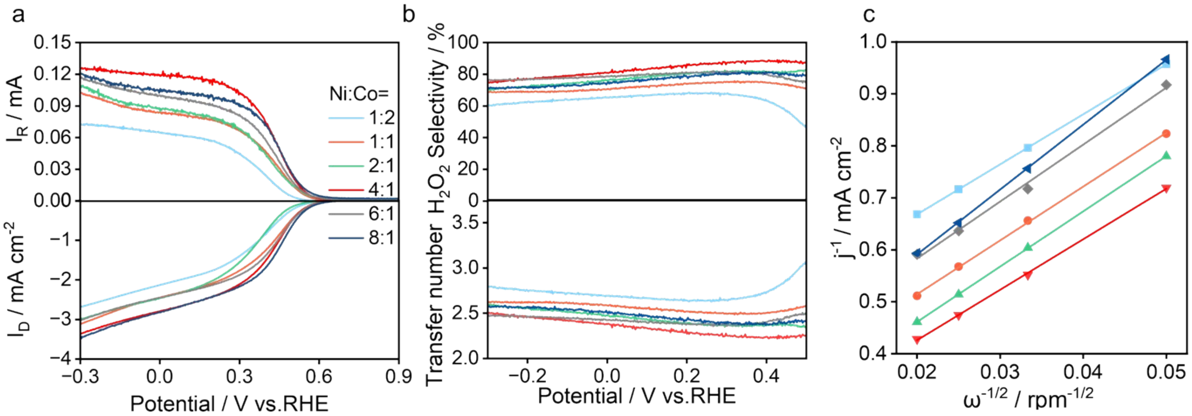

Figure S17. (a) The ORR polarization curves, (b) H_2O_2 selectivity and electron number and (c) Corresponding Koutecky-Levich plots at 0.30 V vs. RHE of $CoNiO_x$ with different Ni/Co ratios.

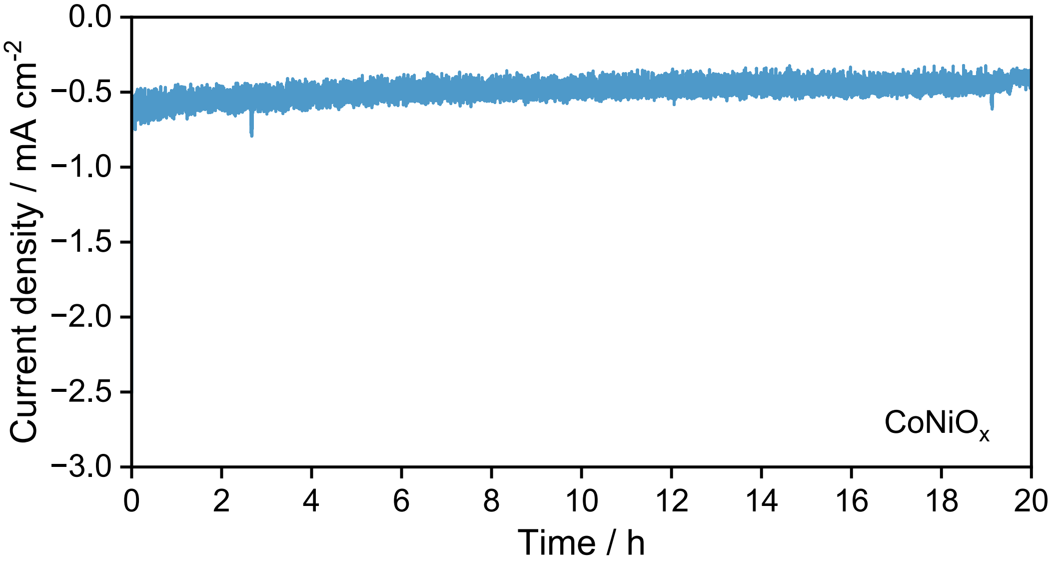

Figure S18. The catalytic stability of CoNiO$_x$ obtained on RRDE at the rotation speed of 0 rpm in 0.10 mol L^{-1} Na$_2$SO$_4$ electrolyte. Note: The disk potential was held at 0.30 V vs. RHE, the ring potential was under open-circuit conditions.

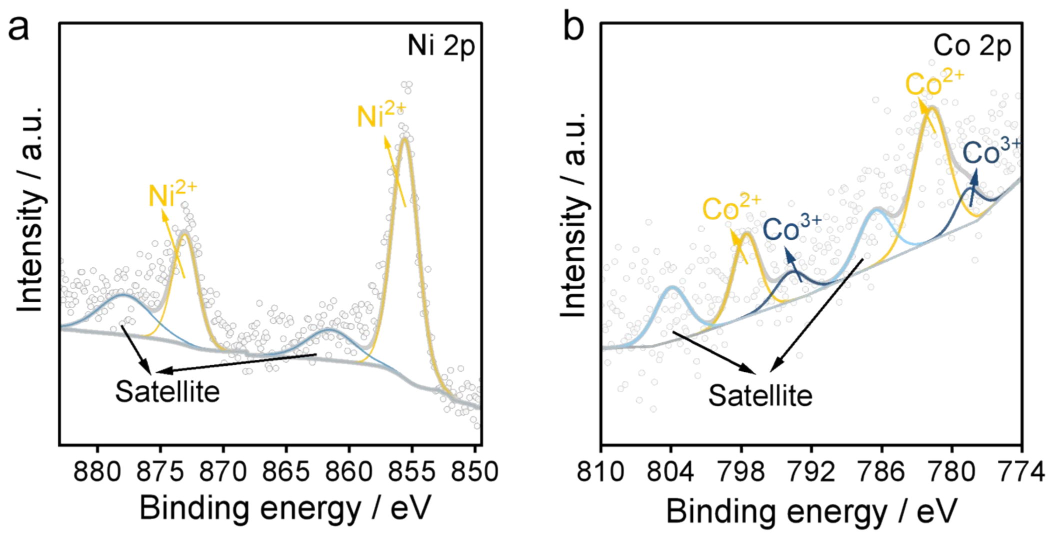

Figure S19. The XPS of CoNiO$_x$ after the electrolysis. Co 2p (a) and Ni 2p (b) XPS spectra of CoNiO$_x$ (4:1).

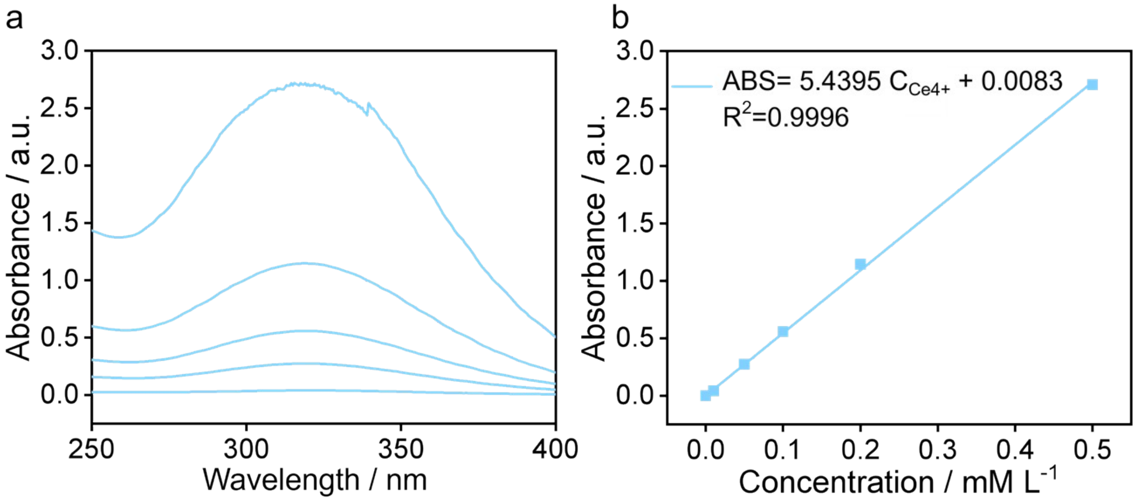

Figure S20. (a) UV-Vis absorption spectra for the determination of Ce^{4+} and (b) Calibration curve.

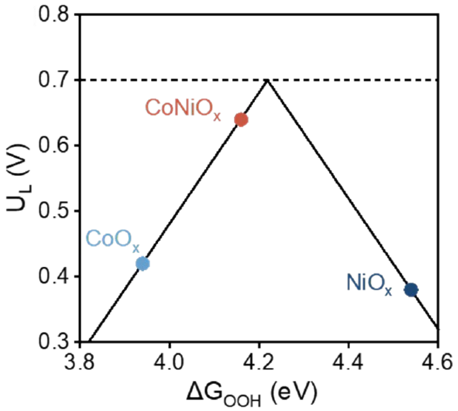

Figure S21. Volcano-type relationship between limiting potential (U_L) and *OOH adsorption energy for $2e^-$ ORR.

The selectivity of the $2e^-$ ORR is generally governed by the adsorption strength of the *OOH intermediate. Overly strong *OOH binding tends to promote O-O bond cleavage and shift the reaction toward the $4e^-$ pathway, whereas overly weak binding hinders *OOH formation and results in sluggish kinetics. Therefore, ΔG_{OOH} is widely used as a descriptor and typically exhibits a volcano-type relationship with the limiting potential (UL). As shown in Fig. S21, CoO_x lies on the left side of the volcano (negative ΔG_{OOH}, strong adsorption), NiO_x on the right side (positive ΔG_{OOH}, weak adsorption), whereas $CoNiO_x$ tunes ΔG_{OOH} closer to the optimal region, consistent with the improved $2e^-$ ORR performance of the experimentally optimized $CoNiO_x$ catalyst relative to CoO_x and NiO_x.

Table S1. Mass fractions of Ni and Co in different $CoNiO_x$ catalyst

Ni/Co ratio	Feed ratio (Ni/Co)	Ni / wt%	Co / wt%
CoO_x	-	0	7.92
$CoNiO_x$ (1:2)	1:2	3.24	4.20
$CoNiO_x$ (1:1)	1:1	3.68	3.38
$CoNiO_x$ (2:1)	2:1	4.54	3.72
$CoNiO_x$ (4:1)	4:1	5.12	3.60
$CoNiO_x$ (6:1)	6:1	6.44	2.80
$CoNiO_x$ (8:1)	8:1	6.94	2.46
NiO_x	-	11.24	0

Catalysts	Electrolyte (neutral, 0.1 M Na_2SO_4)	H_2O_2 Selectivity / %	$E_{1/2}$ / V vs. RHE	References
Co_1-NG(O)	0.1 M PBS	66%	0.30	[7]
IS-NiOC	0.1 M PBS	82%	0.25	[8]
O-CNTs	0.1 M PBS	85%	0.30	[9]
B-C	0.1 M Na_2SO_4	80%	0.30	[10]
700-BNC	0.5 M K_2SO_4	70%	0.10	[11]
Fe/NCNSs	0.1 M PBS	81.9%	0.10	[12]
Co/NCNSs	0.1 M PBS	69.2%	0.15	[12]
Ni/NCNSs	0.1 M PBS	65.0%	0.20	[12]
Cu/NCNSs	0.1 M PBS	70.4%	0.28	[12]
h-SnO_2	0.1 M Na_2SO_4	99.9%	0.35	[13]
SnO_2/COF	0.5 M Na_2SO_4	95.8%	0.25	[14]
VOPc/GCNT-OH	0.5 M Na_2SO_4	90%	0.35	[15]
Fe_M-ZnO	0.1 M PBS	88%	0	[16]
$CoNiO_x$	0.1 M Na_2SO_4	88.9%	0.45	This work

Table S2. H_2O_2 selectivity of various catalysts in neutral electrolyte

References

1 B. Delley, J. Chem. Phys., 2000, 113, 7756–7764.

2 B. Delley, J. Chem. Phys., 1990, 92, 508–517.

3 S. Grimme, J. Antony, S. Ehrlich and H. Krieg, J. Chem. Phys., 2010, 132, 154104.

4 S. Grimme, J. Comput. Chem., 2004, 25, 1463–1473.

5 B. Delley, Mol. Simul., 2006, 32, 117–123.

6 A. Klamt and G. Schüürmann, J. Chem. Soc., Perkin Trans. 2, 1993, 799–805.

7 E. Jung, H. Shin, B.-H. Lee, V. Efremov, S. Lee, H. S. Lee, J. Kim, W. Hooch Antink, S. Park, K.-S. Lee, S.-P. Cho, J. S. Yoo, Y.-E. Sung and T. Hyeon, Nat. Mater., 2020, 19, 436–442.

8 W. Xu, Z. Liang, S. Gong, B. Zhang, H. Wang, L. Su, X. Chen, N. Han, Z. Tian, T. Kallio, L. Chen, Z. Lu and X. Sun, ACS Sustainable Chem. Eng., 2021, 9, 7120–7129.

9 Z. Lu, G. Chen, S. Siahrostami, Z. Chen, K. Liu, J. Xie, L. Liao, T. Wu, D. Lin, Y. Liu, T. F. Jaramillo, J. K. Nørskov and Y. Cui, Nat. Catal., 2018, 1, 156–162.

10 Y. Xia, X. Zhao, C. Xia, Z.-Y. Wu, P. Zhu, J. Y. Kim, X. Bai, G. Gao, Y. Hu, J. Zhong, Y. Liu and H. Wang, Nat. Commun., 2021, 12, 4225.

11 B. N. Ruggiero, X. K. Lu, B. Lu, A. E. Deberghes, D. Nordlund, J. M. Notestein and L. C. Seitz, J. Mater. Chem. A., 2024, 12, 27311–27326.

12 C. Ye, Y. Zhou, H. Li and Y. Shen, Green Chem., 2023, 25, 3931–3939.

13 Y. Zhang, M. Wang, W. Zhu, M. Fang, M. Ma, F. Liao, H. Yang, T. Cheng, C. Pao, Y. Chang, Z. Hu, Q. Shao, M. Shao and Z. Kang, Angew. Chem. Int. Ed., 2023, 62, e202218924.

14 G. Wang, Z. Bao, Y. Li, Y. Wang, X. Cui, H. Zhong, W. Fang and J. Wang, J. Mater. Chem. A., 2025, 13, 6059–6066.

15 H. Yang, N. Guo, S. Xi, J. Yin, T. Song, Y. Xiao, L. Duan, C. Zhang and L. Wang, Angew. Chem. Int. Ed., 2025, 64, e202509079.

16 X. Chai, R.-T. Gao and L. Wang, Chem. Eng. J., 2024, 484, 149527.